RESEARCH ARTICLE

WILEY

Numerical and experimental verification of an inverse-direct approach for load and strain monitoring in aeronautical structures

Luca Colombo[1] | Claudio Sbarufatti[1] | Luca Dal Bosco[1] | Davide Bortolotti[1] | Michal Dziendzikowski[2] | Krzysztof Dragan[2] | Franco Concli[3] | Marco Giglio[1]

[1]Dipartimento di Meccanica, Politecnico di Milano, Milan, Italy

[2]Airworthiness Division, Air Force Institute of Technology, Warsaw, Poland

[3]Faculty of Science and Technology, Libera Università di Bolzano, Bolzano, Italy

Correspondence
Luca Colombo, Dipartimento di Meccanica, Politecnico di Milano, via La Masa 1, Milan, Italy.
Email: luca1.colombo@polimi.it

Summary

Aeronautical structures are increasingly aging, and the occurrence of unexpected loads could reduce their operability. A health and usage monitoring system would enable the continuous monitoring of the state of health of a structure and track its aging by a load monitoring system, which aims at the real-time reconstruction of the loads acting on a structure. However, sometimes the loads and the induced strain and stress fields are difficult to be reconstructed exactly, as for complex loading due to flight maneuvers. In this work, the full strain and load fields of a structure are reconstructed by an inverse-direct approach, leveraging on the calibration matrix approach. The latter exploits a least-squares minimization of an error functional, defined as the comparison between measured strains in discrete positions and a numerical formulation of the same, to reconstruct an equivalent, however representative, load set. By assuming a linear relationship between strain and load through a calibration matrix, this minimization can be performed analytically, leading to a computationally very efficient algorithm that can be operated online. Once the equivalent load set is computed, the full strain field can be estimated relying on a second calibration matrix linking the external loads to the strain field of the complete structure. The method has been numerically tested with an unmanned aerial vehicle (UAV) subjected to aerodynamic pressure loads simulating flight maneuvers. Finally, the results are experimentally validated during a ground test program on a real UAV, proving the robustness to different experimental uncertainties.

KEYWORDS
calibration matrix, equivalent load, inverse problem, load monitoring, strain, usage monitoring

1 | INTRODUCTION

In the last decades, the research on health and usage monitoring systems (HUMS) is driven by the need for aircraft operational life extension. HUMS is intended to monitor the health state of a structure and its consumed life, based on a series of permanently installed sensors.[1-3] In this framework, knowledge of the real load spectra[4] to which a structure

is subjected during its service life and thus the associated strain and stress fields are mandatory for computing the consumed life and exploiting HUMS system data on real structures.[5–7] Thus, load monitoring is a requirement for aircrafts to promote the switch from the *safe-life* design to the *damage-tolerant* concept[8] since it allows continuous monitoring of the structure.

Different load monitoring approaches exist in the literature, either training-based or training-free. Training-based load monitoring makes wide use of machine learning (ML) techniques relying on a series of data, either real or simulated, collected in different scenarios to predict the most likely flight maneuvers[9] or to define mathematical models linking different input parameters to the load estimate, for example, strains and stresses[10] or forces[11] in discrete positions. The latter is usually implemented by exploiting either artificial neural network (ANN)[12,13] or Gaussian process (GP) regression models.[11,14] However, both of them require a training data set, which highly influences the quality of their estimate. A considerable amount of data is usually required to provide a good estimate and to assure a proper input–output space exploration. Training-free load monitoring techniques, on the other hand, do not require a training data set since they rely mainly on a physical model of the structure to estimate the loading condition based on some physical input parameter, for example, strain measures in discrete positions. Some of them[15,16] consider the modal response of the structure to link the strain measures in discrete locations to the strain estimate in predetermined positions of the component. However, difficulties in the strain prediction arise when structures with closely spaced mode shapes are considered, thus limiting their applicability to a case-by-case analysis. Some[17–19] exploit regressions between the excitation source and some residuals to identify the load but suffer from computational resources demand when a high number of degrees of freedom is present in the considered structure. Others,[20–24] falling under the category of shape sensing, aim at reconstructing the full displacement and thus, strain, fields of a structure based on a least-squares minimization of an error functional defined as a comparison between discrete strain measurements and a numerical formulation of the same without requiring any a priori knowledge of the load boundary condition and the material properties. However, the latter are limited to date to plates and beam-like structures discretized with inverse finite elements method (iFEM). Another method, sometimes referred to as the calibration matrix approach, reconstructs a set of loads minimizing an error functional comparing discrete strain measures with a numerical formulation of the same, function of the unknown loads. Many applications can be found in the literature of the calibration matrix approach spanning from railway transportation leveraging on the wheel-rail contact force[25,26] to civil and aeronautical applications either at a numerical level[27,28] or experimentally.[29–33]

However, even though the general framework of the calibration matrix approach is already available for estimating loads at a global level, for example, total lift and drag, few applications can be found in the literature of the use of the method for full strain reconstruction of aerodynamic flight maneuvers exploiting a numerical model of the complete structure. In particular, once a calibration matrix linking the strain in discrete positions to an equivalent load set representative of the real load condition is computed based on an FEM of the structure, the full strain field can be estimated exploiting an inverse-direct approach. Indeed, after the equivalent load set is computed by a least-squares approach, the full strain field can be reconstructed by simple matrix–vector multiplication, assuring real-time operability at a reduced computational burden.

The method is numerically verified with a full-scale Unmanned Aerial Vehicle (UAV) loaded by different aerodynamic pressure fields simulating aircraft flight maneuvers to demonstrate the method applicability for full strain field reconstruction. An on-ground experimental verification is also performed to consider possible disturbances and to deal with possible model-reality discrepancies.

The paper is structured as follows. A comprehensive mathematical description of the calibration matrix approach is provided in Section 2. The UAV structure, the model, the sensor network, and the equivalent load set used for full strain and load reconstruction are described in Section 3. Then, the results of both the numerical and experimental tests are presented in Section 4. Finally, a conclusive section is provided.

2 | MATHEMATICAL FRAMEWORK

A comprehensive description of the mathematical framework of the proposed load monitoring approach is provided in this section, clarifying some steps not fully detailed in the literature for the interested reader.

Suppose a structure is subjected to an unknown and arbitrary load, L_u. As a direct consequence of the load L_u, the structure undergoes a unique deformation, resulting in a strain field ε_u function of the load L_u itself.

Consider the same structure is instrumented with n_s sensors measuring the deformation at n_s discrete positions, $\boldsymbol{x}_s$, within the component and the measures at the time instant t are collected in a $n_s \times 1$ vector $\boldsymbol{\varepsilon}$:

$$\boldsymbol{\varepsilon} = \left\{ \begin{array}{c} \varepsilon_1 \\ \vdots \\ \varepsilon_{n_s} \end{array} \right\} \tag{1}$$

The external loads, expressed as a series of n_{lr} discrete real loads, or a simplified equivalent representative version, are computed through a least-squares approach by minimizing an error functional e, defined as the comparison between measured strain, $\boldsymbol{\varepsilon}^m$, and a numerical formulation of the same, $\boldsymbol{\varepsilon}^n$, function of the load (or equivalent load) set, $\boldsymbol{F}$:

$$e(\boldsymbol{F}) = (\boldsymbol{\varepsilon}^m - \boldsymbol{\varepsilon}^n(\boldsymbol{F}))^2 = (\boldsymbol{\varepsilon}^m - \boldsymbol{\varepsilon}^n(\boldsymbol{F}))^T (\boldsymbol{\varepsilon}^m - \boldsymbol{\varepsilon}^n(\boldsymbol{F})) \tag{2}$$

By assuming a linear-elastic behavior of the structure, which is plausible in many engineering applications, the ith strain measure, ε_i, in the vector $\boldsymbol{\varepsilon}^n$ can be written as follows:

$$\varepsilon_i = \varepsilon_i^1 + \varepsilon_i^2 + ... + \varepsilon_i^{n_{lr}} = \sum_{j=1}^{n_{lr}} \varepsilon_i^j \tag{3}$$

where ε_i^j is the strain in position $\boldsymbol{x}_i$ when only the jth load is acting on the structure.

Furthermore, a linear relationship exists between the load and the strain such that

$$\varepsilon_i^j = \alpha_{ij} F_j \tag{4}$$

in which the α_{ij} term is the strain-force proportionality factor, often referred to as "influence" or "calibration" coefficient.

By considering all the n_s strain measures together, the relation in Equations 3 and 4 can be written in vector form as

$$\boldsymbol{\varepsilon}^n(t) = \boldsymbol{\varepsilon}^1(t) + \boldsymbol{\varepsilon}^2(t) + ... + \boldsymbol{\varepsilon}^{n_{lr}}(t) = \sum_{j=1}^{n_{lr}} \boldsymbol{\varepsilon}^j(t) = \sum_{j=1}^{n_{lr}} \boldsymbol{\alpha}^j F_j(t) = \boldsymbol{\alpha} \boldsymbol{F}(t) \tag{5}$$

where $\boldsymbol{F}$ is a $n_{lr} \times 1$ vector containing all the loads that one aims to reconstruct at the time t and hereon referred to as load (or equivalent load) vector

$$\boldsymbol{F} = \left\{ \begin{array}{c} F_1 \\ \vdots \\ F_{n_{lr}} \end{array} \right\} \tag{6}$$

while $\boldsymbol{\alpha}$ is a $n_s \times n_{lr}$ proportionality matrix, from here onward referred to as calibration matrix, containing the proportionality or influence coefficients between strain and load:

$$\boldsymbol{\alpha} = \begin{bmatrix} \alpha_{11} & \cdots & \alpha_{1n_{lr}} \\ \vdots & \ddots & \vdots \\ \alpha_{n_s 1} & \cdots & \alpha_{n_s n_{lr}} \end{bmatrix} \tag{7}$$

Notice that each α_{ij} component of the $\boldsymbol{\alpha}$ matrix can be interpreted as the strain in the position $\boldsymbol{x}_i$ that one reads if a single unitary force j is acting on the structure. Thus, the calibration matrix is constructed column by column by activating one unitary load per time among the possible set of equivalent loads $\boldsymbol{F}$. The $\boldsymbol{\alpha}$ matrix can also be interpreted as the linear operator mapping loads in the load space into deformation in the strain space.

By plugging Equation 5 in the error functional of Equation 2, the error functional formulation becomes as follows:

$$e = (\boldsymbol{\varepsilon}^m - \boldsymbol{\alpha}\boldsymbol{F})^T(\boldsymbol{\varepsilon}^m - \boldsymbol{\alpha}\boldsymbol{F}) = \boldsymbol{\varepsilon}^{mT}\boldsymbol{\varepsilon}^m - \boldsymbol{\varepsilon}^{mT}\boldsymbol{\alpha}\boldsymbol{F} - \boldsymbol{F}^T\boldsymbol{\alpha}^T\boldsymbol{\varepsilon}^m + \boldsymbol{F}^T\boldsymbol{\alpha}^T\boldsymbol{\alpha}\boldsymbol{F} \tag{8}$$

Finally, by minimizing the error with respect to the unknown vector of the equivalent loads, $\boldsymbol{F}$

$$\frac{\partial e}{\partial \boldsymbol{F}} = 0 \tag{9}$$

the solution of the inverse problem is found as follows:

$$\boldsymbol{\alpha}^T\boldsymbol{\alpha}\boldsymbol{F} - \boldsymbol{\alpha}^T\boldsymbol{\varepsilon}^m = \boldsymbol{0} \tag{10}$$

or simply

$$\boldsymbol{F} = \left(\boldsymbol{\alpha}^T\boldsymbol{\alpha}\right)^{-1}\boldsymbol{\alpha}^T\boldsymbol{\varepsilon}^m = \boldsymbol{\alpha}^+\boldsymbol{\varepsilon}^m \tag{11}$$

being $\boldsymbol{\alpha}^+$ the Moore–Penrose inverse or pseudo-inverse matrix of the calibration matrix $\boldsymbol{\alpha}$.

It is worth noticing that the $n_s \times n_{lr}$ calibration matrix $\boldsymbol{\alpha}$ is usually not squared (i.e., $n_s \neq n_{lr}$), and for the inverse problem to be solvable, one has to verify that the matrix $\boldsymbol{\alpha}^T\boldsymbol{\alpha}$ is invertible, which results in the following requirement:

$$rank(\boldsymbol{\alpha}) = n_{rl} \tag{12}$$

Equation 12 contains the sensor network requirements for a load monitoring system. In fact, not only must the sensors be at least n_{lr} for the problem to be determined, but they also have to be placed[34–36] in a way that they provide different information for each load in the equivalent load set; that is, the columns of the calibration matrix must be linearly independent. Furthermore, Equation 12 enables the introduction of the concept of observability requirement for the inverse problem. Indeed, since the load monitoring algorithm aims to reconstruct the unknown equivalent load set, $\boldsymbol{F}$, based on sensors' discrete strain measures, one has to be sure that the network guarantees the "observability," that is, the load reconstruction, prior to the real on-board installation. Hereafter, ensuring that the calibration matrix's rank is equal to the number of loads, n_{lr}, results in the satisfaction of the observability requirement before the actual implementation of the load monitoring system on the structure.

Once the equivalent load set $\boldsymbol{F}$ is reconstructed through Equation 11 at each time instant t, the full strain field, $\boldsymbol{\varepsilon}_{field}$, can be estimated by applying a direct approach, as described in Equation 13:

$$\boldsymbol{\varepsilon}_{field} = \boldsymbol{\alpha}_{field}\boldsymbol{F} \tag{13}$$

where $\boldsymbol{\alpha}_{field}$ is another calibration matrix linking the equivalent load set $\boldsymbol{F}$ to the quantity of interest in the monitored areas, which, in the most general case, can include the entire structure. In particular, the columns of $\boldsymbol{\alpha}_{field}$ are still n_{lr}, but the number of rows becomes equal to the number of positions to be monitored. The extrapolated strain field can be exploited in additional algorithms (e.g., for anomaly identification), and, since the optimization procedure is performed on the strain, the latter can be recovered quite accurately also in the case of nonideal behavior of the structure. In the last case, one should consider some loss of accuracy in load reconstruction. However, once the strain field is available online and offline, further refinement of the load reconstruction algorithm is possible.

Furthermore, it is worth noticing that both the inverse step, for the load estimation, and direct step, for the full strain field reconstruction, involve just matrix–vector multiplications, resulting in a very efficient algorithm that can be operated online, since the pseudo-inverse matrix $\boldsymbol{\alpha}^+$ is computed just once offline.

3 | THE CASE STUDY

The case study for the load monitoring methodology described in Section 2 is presented in this section. In particular, the strategy for applying the load monitoring algorithm to an UAV is presented in Section 3.1. The aeronautical structure considered in this work as a bench test is briefly described in Section 3.1.1, while the numerical model of the UAV used for the structural simulation is shown in Section 3.1.2. The realistic aerodynamic load scenario, representative of the flight maneuvers, is described in Section 3.1.3, while the simplified equivalent load set processed by the load monitoring algorithm is introduced in Section 3.1.4. Finally, the strain sensor network installed on the structure is described in Section 3.2.

3.1 | Load monitoring strategy for an UAV

The load monitoring strategy is applied on a full-scale UAV described in Section 3.1.1. In particular, the UAV is tested both numerically and experimentally, relying on a numerical structural model. Since the experimental test rig is bounded by previous static tests on the structure which required the use of four saddles mounted on the two wings and loaded by concentrated forces as well as fixing of the aircraft to a support structure through some connecting elements, the numerical model is built accordingly.

Furthermore, it is widely recognized that aeronautical structures are subjected to aerodynamic loads during their operation. However, supppose one wants to test the UAV before its operational deployment. In that case, it is neither easy nor economical to load the structure by aerodynamic pressure fields. Thus, the use of lumped loads representative of the flight maneuvers is usually a practical alternative to expensive wind tunnel sessions. In this work, the value of the lumped loads is calculated using the calibration matrix approach with a simulated set of discrete strain measures in the sensor positions obtained from a computational fluid dynamics (CFD) software when simulating flight maneuvers. The obtained equivalent load set, F, represents both the considered flight maneuver and the complete strain field in the structure caused by the maneuver itself and can be further exploited for the computation of the consumed life.

Once the numerically equivalent load sets are computed from the simulated flight maneuvers, this realistic loading condition is used for the experimental verification of the method, proving the possibility of reconstructing the external loads and the localized strains in the presence of experimental uncertainties.

3.1.1 | The UAV

The load monitoring methodology described in Section 2 is tested on a full-scale UAV employed as an aerial target during military training sessions of the Polish Air Force, namely, the Hornet.[37] The UAV, shown in Figure 1, is a modified version of the originally developed structure, designed and manufactured by the Air Force Institute of Technology (AFIT) and the Military Aviation Works No. 1 (MAW1). In particular, the Hornet is made of composite material (mainly glass fiber [FB]) with a length of about 1.7 m, a wingspan of about 3.2 m, and capable of reaching a maximum speed of about 230 km/h. Further specifications are reported in Table 1. Specifically, this work focuses on the wing of the UAV, which is made of two main spars and three ribs glued on the two skins of the wing. All these main parts are made of composite material with sandwich structures formed in negative molds using vacuum techniques. The wings are then connected to the fuselage using a circular beam made of Dural.

FIGURE 1 The UAV

Parameter	Value
Length	1.7 m
Wing span	3.2 m
Starting weight	38 kg
Fuel tank capacity	8 L (6.3 kg)
Useful weight (payload)	5 kg
Min–cruise–max speed	$85 - 150 - 230$ km/h
Operating range	40 km
Maximum climbing speed	16 m/s (at 140 km/h)

TABLE 1 UAV technical specifications

3.1.2 | The UAV FEM

As described in Section 2, the inverse problem is tackled using a calibration matrix α linking loads and deformation. The influence coefficients α_{ij} in α are numerically computed exploiting the FEM of the structure shown in Figure 1. The UAV's structural model, developed in ABAQUS, is a slight simplification of the real aircraft in which the overall structural behavior of the Hornet in terms of strain patterns is not compromised. Indeed, although the internal combustion engine, the propeller, the most complicated fasteners, and slivers have not been modeled, the structural response is correctly captured. This structural response has been confirmed by a previously performed experimental validation of the overall strain field and the particular strain field in the two wings, focus of the present study. Furthermore, since the current work is not aimed at the modeling of the interaction between different components in the structure, linear constraints have been used to connect the different regions of the aircraft. An overview of the FEM is shown in Figure 2.

The UAV in the previously performed static tests was supported by a rigid frame shown in Section 3.1.4. Thus, a clamp boundary condition was imposed in the FE model (Figure 3) at the interface regions between the UAV and the supporting frame. The latter is considered infinitely rigid and thus not modeled.

Notice that, since the focus of the work is on the two wings, adopting a rigid clamp at the interface between the frame and the aircraft fuselage will not affect the results in the analyzed area, being the latter far from the boundaries. Furthermore, although the adoption of linear constraints for connecting the different parts of the UAV may result in a localized increase of stiffness and imprecise modeling of the interfaces' structural behavior at small loads, the structure's overall behavior is correctly captured. In particular, excellent agreement is found with operational loads impacting the structural integrity.[38]
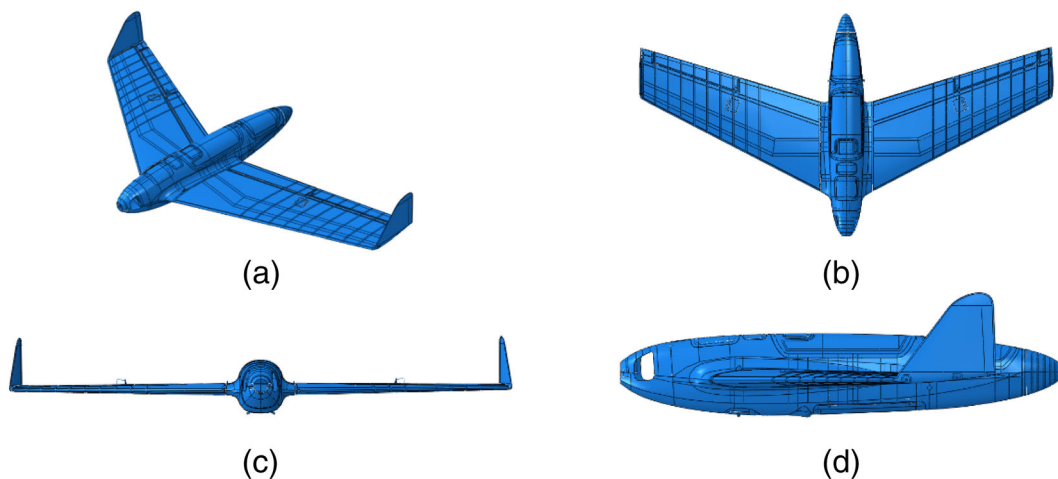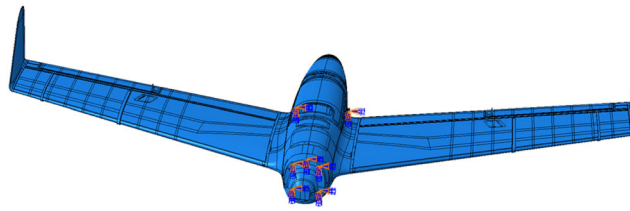

(a)

(b)

(c)

(d)

FIGURE 2 The UAV finite element model; (a) FEM overview; (b) FEM top view; (c) FEM front view; (d) FEM lateral view

3.1.3 | The simulated aerodynamic pressure field

Different loading conditions in terms of varying aerodynamic pressure fields are applied to the FEM to verify in a simulated environment the ability of the method to correctly reconstruct the full-strain field $\boldsymbol{\varepsilon}_{field}$, even in locations not considered for the input strain measures, $\boldsymbol{\varepsilon}^m$. In particular, a total of 1,440 aerodynamic CFD simulations with varying parameters performed through the PANUKL[39] software are considered to simulate a realistic loading conditions the UAV might undergo during operation maneuvers. Assuming small displacements of the structure during operation, the CFD and FE simulations have been separated, thus computing the aerodynamic pressures on the infinitely rigid structure and then applying the resulting pressures on the deformable FE model.

The complete set of flight parameters simulating different flight manoeuvers is reported in Table 2. For brevity and without any loss of generality, only the results with 55 m/s flight speed, 5° angle of attack, and 5° left and right aileron deflections are shown in this work, corresponding to the aerodynamic pressure field reported in Figure 4.
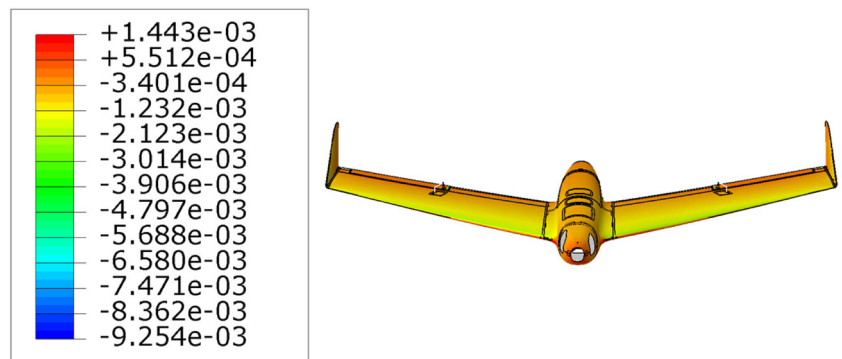
3.1.4 | The equivalent load set

As the inverse reconstruction of the aerodynamic pressure distribution is not practical due to the high number of variables, the matrix-based load monitoring method requires the definition of an equivalent load set, $\boldsymbol{F}$, optimized in a way that the strain distribution along the structure has a limited error compared to the one associated to the real loading condition. In this study, aiming the on-ground validation of the method with static lumped loads, $\boldsymbol{F}$ is defined as four concentrated forces applied on some locations where saddles are mounted on the Hornet's wings, as shown in Figure 5b. The saddles, modeled in the FEM as in Figure 5a, distribute the forces along the wing chord, originating a

TABLE 2 The CFD simulations parameters

Parameter	Min.	Max	Step	N° of levels
Flight speed	20 m/s	60 m/s	5 m/s	9
Angle of attack	−5°	10°	1°	16
Left aileron deflection	−10°	20°	5°	7
Right aileron deflection	−10°	20°	5°	7

FIGURE 4 Aerodynamic pressure field in [MPa] for a flight speed of 55 m/s and an angle of attack, left and right aileron deflection of 5°
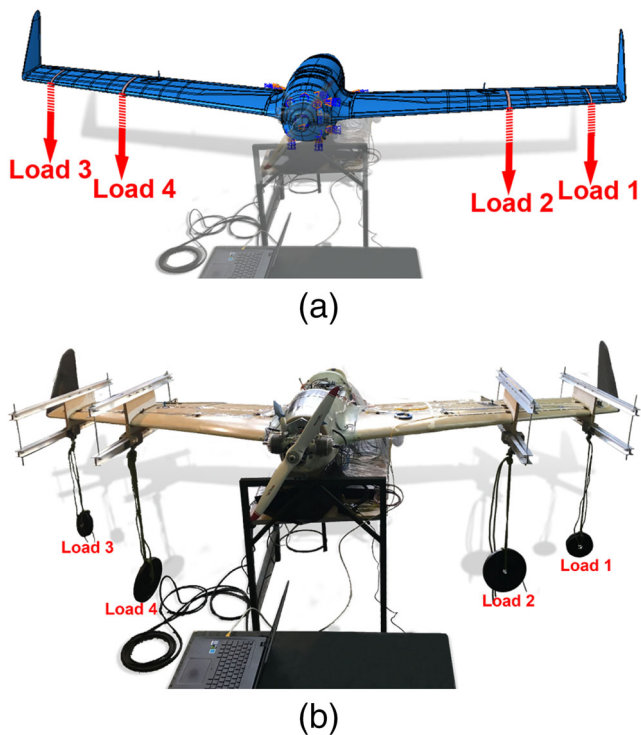
FIGURE 5 Equivalent load set definition; (a) FEM concentrated forces acting on the saddles; (b) experimental setup with four forces applied symmetrically on the wings

lumped pressure distribution. As demonstrated in Section 4, this simplification of the load condition produces a limited error in the reconstructed strain distribution, at least far from the discontinuity regions where the load is applied. Finally, as detailed in Section 4.2, the magnitude of the forces in F during validation was selected to represent flight maneuvers associated with the aerodynamic pressures fields described in Section 3.1.3.

3.2 | The strain sensor network

The last step before implementing the matrix-based load monitoring system is the definition of a strain sensor network for the input measures, ε^m. In particular, two different types of networks are numerically and experimentally defined, namely, the input sensor network and the test sensors network. The former is used as input to the load monitoring algorithm. The latter serves as verification for the strain field reconstruction based on the inverse-direct approach.

3.2.1 | The input sensors network

A set of $n_s = 20$ sensors positioned symmetrically between left and right wings was defined in the FEM based on the observability requirement and engineering judgment, as shown in Figure 6a. In particular, the sensors were positioned to consider at least one sensor in each bay created by the saddles. This setup ensures that the different forces have a different effect on the sensors and, thus, that $rank(\alpha) = 2$. Although a symmetrical loading was performed to avoid that the UAV would accidentally overturn due to the structure's symmetry and without loss of generality, the experimental validation of the method was performed by instrumenting one wing of the UAV and, thus, considering only its relative sensor measures. An optical FB equipped with 10 fiber Bragg grating (FBG) sensors was installed on the external skin surface of the UAV's left wing in the same positions considered in the FEM, as illustrated in Figure 6b. It is worth noticing that, as defined in Equation 12, the calibration matrix's rank, $rank(\alpha)$, has to be equal to the number of unknowns to be estimated, meaning that at least two sensors should be used to determine the two forces acting on each wing. However, the input sensors cannot be positioned randomly because adhering to the requirement of the minimum number of sensors is not sufficient to guarantee that the observability requirement is satisfied. Indeed, one always has to verify before the sensor installation that the calibration matrix's rank is equal to the number of unknown loads to be reconstructed.

FIGURE 6 The input sensor network for load monitoring. The sensor ID is reported only for the left wing sensor network; (a) sensor network for load monitoring and equivalent force reconstruction in the FEM; (b) sensor network for load monitoring and equivalent force reconstruction in the real UAV structure

(a)

(b)
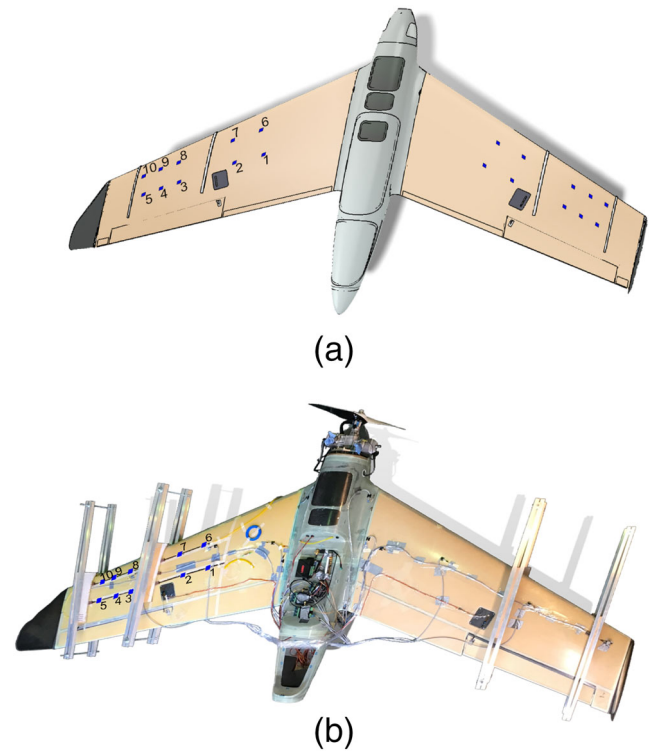
3.2.2 | The test sensors network

Two different test sensor networks are used for the numerical (a) and experimental (b) verification of the method.

The method's abilities (i) to reconstruct a strain field similar to that originated by the aerodynamic pressure field exploiting the equivalent lumped load sets and (ii) to extrapolate strain information in positions not seen as input are numerically verified by defining (a) eight virtual optical FBs in correspondence of critical structural elements of both wings, that is, the spar and the skin, as illustrated in Figure 7. In particular,

- FB1, FB2, FB5, and FB6 are defined on the top and bottom of the two wings spars
- FB3, FB4, FB7, and FB8 are defined on the top and bottom of the two wings skins.

The FBs are used as testing positions, ε_t, for the reconstructed strain field, ε_{field}, and are not included in the strain input vector, ε^m. Thus, the vector of test strains, ε_t, simulates the strain values a physical sensor would measure if subjected to the considered flight maneuver and has to be compared with the strain reconstructed by the algorithm, ε_{field}.
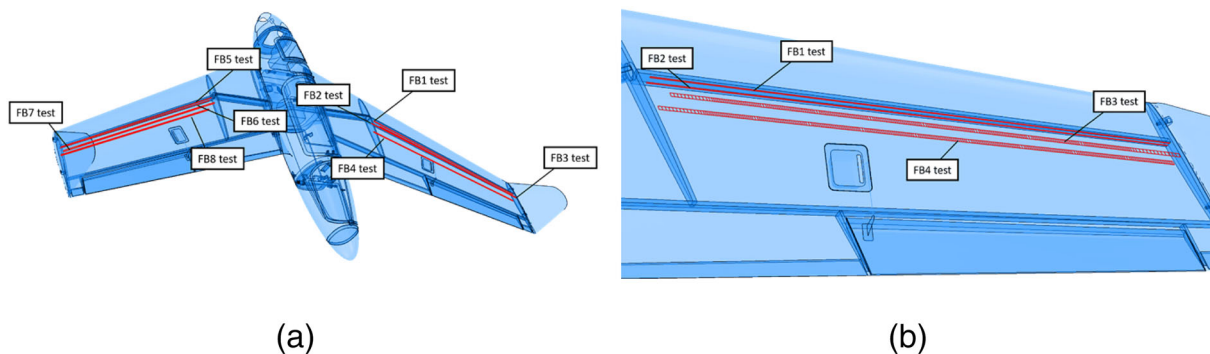

(a)

(b)

FIGURE 7 Test sensors network; (a) overall view; (b) detail of the right wing

Due to experimental limitations, a limited sensor network is used to experimentally verify the methodology, specifically considering (b) subsets of the available sensor network as ε^m and using the remaining sensors as testing positions, ε_t. An example of the experimental input and test subsets is shown in Figure 8. The red squares refer to the sensors used as input, and the green squares mark the sensors used for testing. Note that, in correspondence to the input strain locations, the input and reconstructed strains can differ due to algorithm smoothing. Thus, in the most general case, the input strain locations can also be part of the test vector.

4 | RESULTS

The results are reported in this section for the UAV structure described in Section 3.1. In particular, the numerical results with the structure subjected to simulated maneuvers are described in Section 4.1, while the experimental verification of the method is reported in Section 4.2.

4.1 | The numerical test

The algorithm is numerically tested by applying the aerodynamic pressure field calculated for one example maneuver, as in Figure 4, over the structural elastic model. The continuous red lines in Figure 9 represent the target strain in the test positions (Figure 7) of the structure subject to aerodynamic load, to be compared with the strain reconstructed by the algorithm in the same test positions. The latter are based on the input sensor grid shown in Figure 6a and the estimated equivalent lumped load set reported in Table 3. Note that the reconstructed equivalent load set values in Table 3 are used in the following experimental validation for loading the UAV during on-ground tests.

The results in Figure 9 show that a good strain reconstruction in positions different than those considered for the equivalent load set reconstruction can be obtained by exploiting a limited number of input measures. Excellent

FIGURE 8 Example of the experimental input and test sensors networks: Red squares mark the sensors used both as input and test; green squares mark the sensors used only as test
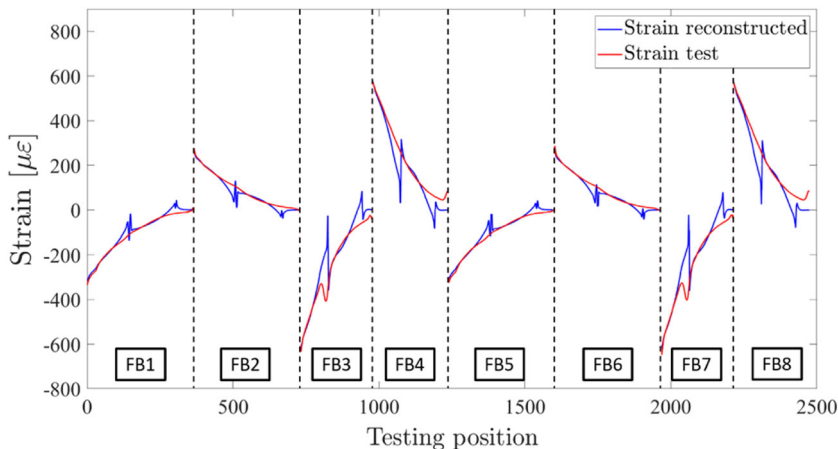

FIGURE 9 Comparison between reconstructed strains, ε_{field} and the strain in the testing positions, ε_t. The testing positions refer to Figure 7

TABLE 3 Equivalent load set reconstruction

	Load 1	Load 2	Load 3	Load 4
Magnitude (N)	49.67	97.58	50.88	98.27

reconstruction of the strain field is found in correspondence of the two spars (FB1, FB2, FB5, and FB6) because they are more rigid than the two skins and, thus, less affected by local effects due to the concentrated loading choice. Indeed, the concentrated loading through the four saddles and the rigid connection between the saddles and the wings cause discontinuities in the reconstructed strain in correspondence of the saddle locations. However, this is limited to the neighboring zone, and thus, the general trend of deformation is correctly captured.

Furthermore, the root mean square error (RMSE) between the reconstructed (ε_{field}) and the test strain (ε_t) has been calculated, obtaining a value of 44.25 $\mu\varepsilon$. Even though the concentrated forces introduce an intensification of the error close to the saddle areas negatively affecting the RMSE, the value of the RMSE remains quite low compared to the maximum level of the strain. Indeed, an error of about 44 $\mu\varepsilon$ over a maximum strain level of about 700 $\mu\varepsilon$ means an error of about 6%, which is acceptable, considering the simplified choice of the equivalent load set compared to the aerodynamic condition. It is worth remarking that most of the error in the strain reconstruction is due to the concentration of the aerodynamic load in only two locations per wing. The concentrated load produces an intensification of the strain due to higher resultant forces than the locally distributed load. Additional localized error is introduced with the rigid connection modeling between the saddles and the wing, which induces an additional deformation of the structure, especially in the wing's low stiffness area. However, the error can be decreased if a distributed lumped load is considered in more positions of the wing, reducing the local intensification effect of simplifying a distributed pressure with concentrated loads.

Finally, a graphical comparison of the full-strain field reconstruction in terms of equivalent strain (Von Mises strain) in the whole UAV structure with respect to the full-strain field generated by the aerodynamic pressure field is shown in Figure 10. A good agreement is observed despite a discretization of the loading condition with only four forces, especially in the wing root region where the strain level is highest. Notice that, despite only a qualitative comparison can be performed considering Figure 10, one can observe that the maximum strain level is obtained in the correct position, and the overall strain distribution is correctly captured, producing encouraging results for further investigations.

4.2 | The experimental verification

The experimental verification of the load monitoring method for the UAV described in Section 3.1 is presented in this section. The UAV is loaded with concentrated forces applied to four saddles exploiting the numerical results presented in Table 3, as anticipated in Section 3.1, to obtain a similar effect of a flight maneuver in terms of strain and displacement fields. Furthermore, since the experimental sensor network has been installed only on the external skin of the left
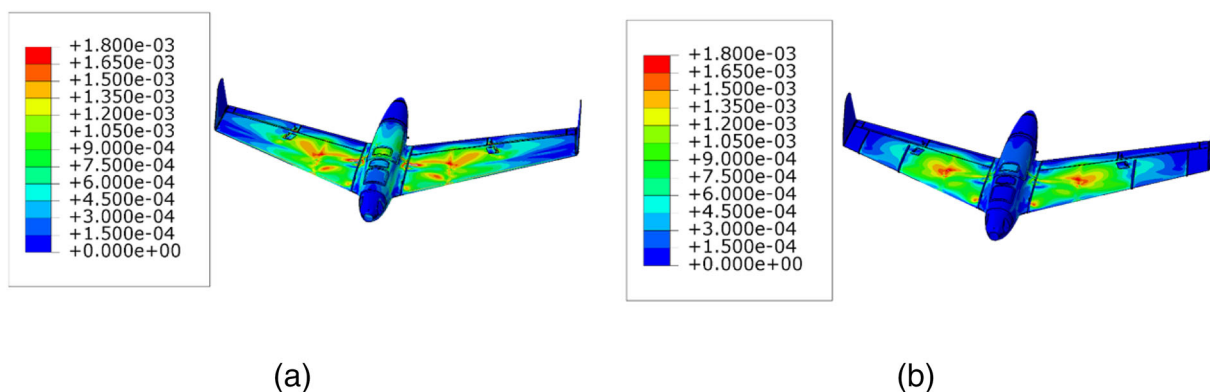

(a)   (b)

FIGURE 10 Full strain field comparison considering a Von Mises strain; (a) test strain field caused by a CFD pressure distribution; (b) reconstructed strain field using equivalent forces

wing due to the symmetry of the structure and independence between the loading in the two wings, only the equivalent Loads 1 and 2 are estimated, although the structure is loaded symmetrically to avoid undesired overturning during the loading (Figure 11).

The load monitoring method's performance was tested analyzing the reconstruction capabilities of different subsets of the experimental sensor network shown in Figure 6b and reconstructing the strains and loads in all the sensor positions available. A reduced calibration matrix, that is, computed from just a few of the available sensors, was defined for each subset of the input sensor network, always verifying that the observability condition is respected, that is, $rank(\boldsymbol{\alpha}) = 2$.

Figure 12 shows the reconstruction results for an input sensors network of six sensors (specifically, sensor ID 1, 2, 3, 6, 7, and 9 in Figure 8) separately for loads and strains. The load reconstruction ability of the method is confirmed by the results of Figure 12a, which particularly demonstrates that the experimental lumped loads can be reconstructed exploiting a sensors network composed of only six sensors also in the presence of experimental uncertainties. Load 1 is slightly underestimated but compensated by a barely visible overestimation of Load 2. This is due to a low effect of the bending moment on the sensors close to Load 1. However, despite these little discrepancies in the load reconstruction, the strain field reconstruction is in excellent agreement with the experimental measures, demonstrating the method robustness also for the full-strain field estimation.

The reconstructed load sets and strains as a function of different input sensor networks are reported in Tables 4 and 5, respectively. The results presented in Table 4 demonstrate that the load estimation accuracy increases with the increase of the number of input sensors. However, the accuracy is already quite good with the minimum amount of sensors. Furthermore, the reconstructions dispersion between different sensor networks decreases, meaning the input sensor network's optimization becomes a critical step for sensor grids with a limited number of sensors. Indeed, the requirement of observability only guarantees that the load can be mathematically estimated; however, the accuracy of the reconstruction depends on the quality and the level of the strain measurements, which can vary point by point on the structure. Table 4 suggests that the observability requirement becomes particularly relevant when the number of input sensors is limited. Indeed, as the results with only two sensors show, only 27 out of 45 possible combinations satisfy the observability condition (i.e., $rank [\boldsymbol{\alpha}] = 2$). This means that 40% of the available sensors' combinations do not allow a reconstruction of the load set. However, the observability requirement can be verified before the actual sensor
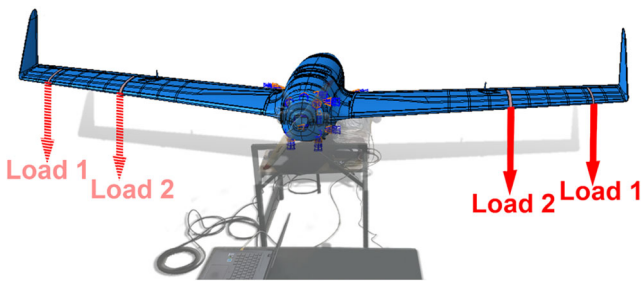

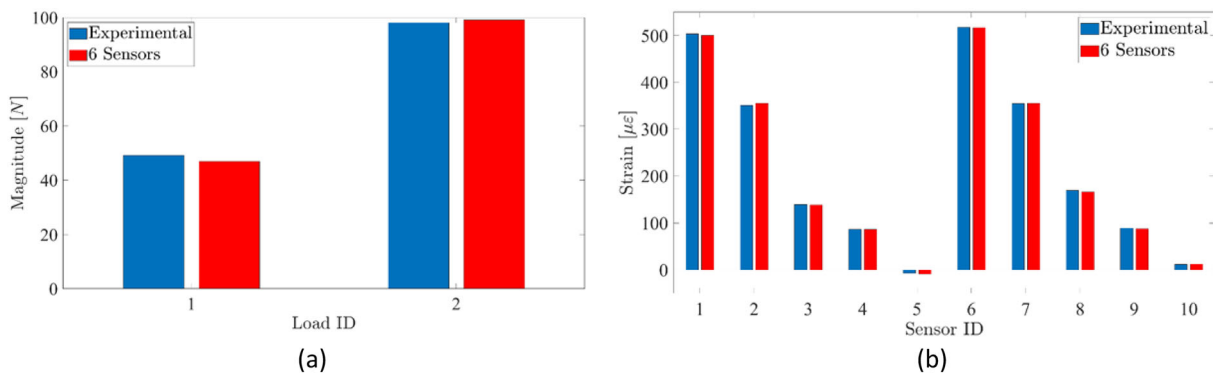**FIGURE 11**   Symmetrical experimental loading

FIGURE 12   Comparison between the experimental value and the average reconstruction with the input sensors network of Figure 8 composed of six sensors; (a) comparison between the experimental and the reconstructed loads; (b) comparison between the measured and the reconstructed strains in the testing positions

TABLE 4 Number of feasible sensor network subsets and average values of Loads 1 and 2 reconstructed considering different subsets of input sensor networks

	No. of unique sensor combinations	No. of sensor combinations with max rank	Load 1 (N)	Load 2 (N)
Experimental values	-	-	**49**	**98**
Reconstructed (2 sensors)	45	27	45.4 ± 3.4	103.5 ± 12.4
Reconstructed (4 sensors)	210	195	46.8 ± 0.9	98.7 ± 4.7
Reconstructed (6 sensors)	210	209	46.8 ± 0.6	99.1 ± 2.9
Reconstructed (8 sensors)	45	45	46.8 ± 0.4	99.6 ± 1.6
Reconstructed (10 sensors)	1	1	46.8 ± 0.4	99.7 ± 1.1

installation to avoid subsequent spoiling of the reconstruction results. Similar results can be noticed in Table 5 for the strain. The dispersion of the strain reconstruction with different sensor grids decreases increasing the number of sensors. In contrast, the reconstruction's accuracy slightly increases, even though a good estimation is achieved for all the cases considered.

Finally, the RMSE is considered to evaluate the reconstruction procedure's performances quantitatively. Figure 13 shows the RMSE results for all the feasible combinations of input sensor networks for the strains and the loads. In particular, the error decreases as far as the number of input sensors increases both in terms of load and strain reconstructions, as shown in Figure 13a. Indeed, the sensor networks characterized by only two sensors are featured by the most significant error. The inverse problem is simply determined. Thus, the results are highly affected by the noise in the input strains, which determines the quality of the load estimation and strain reconstruction. Furthermore, by looking at Figure 13b, one can notice that Load 2 is reconstructed less accurately than Load 1, especially with a low number of input sensors. This is because both loads produce mainly a bending on the wing. Thus, since Load 1 features a bigger arm than Load 2, the former produces higher strain levels, and, during optimization, an error in Load 1 reconstruction has a higher weight that in Load 2. However, the reconstruction's error is quite satisfactory even with a low number of sensors, for example, about 8 *N* over a level of about 100 *N* with only three sensors, meaning less than 10% of error in the loads and even lower for the strains (i.e., about 1%).

TABLE 5 Average values of the reconstructed strain in the testing position as a function of different input sensor networks

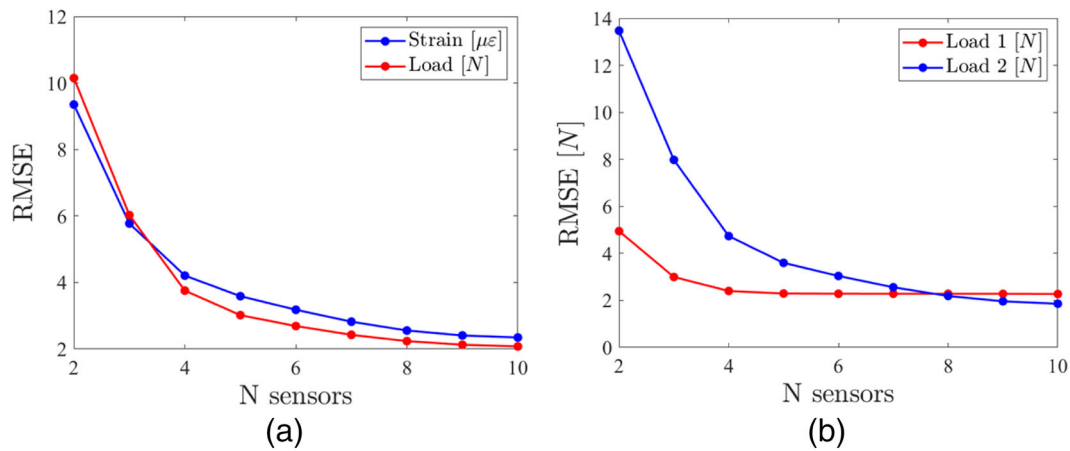|		No. of sensors				
Sensor ID	**Experimental strain (με)**	**2 (με)**	**4 (με)**	**6 (με)**	**8 (με)**	**10 (με)**
1	503.25	501.1 ± 10.9	499.2 ± 6.5	500.1 ± 4	500.9 ± 1.8	501.1 ± 0.9
2	350.84	350 ± 10.7	354.3 ± 3	354.7 ± 2.1	354.8 ± 1.5	354.9 ± 1.3
3	139.55	134.3 ± 10.2	138.6 ± 2.8	138.7 ± 1.8	138.6 ± 1.3	138.5 ± 0.1
4	86.43	84.2 ± 6.4	86.9 ± 1.7	86.9 ± 1.1	86.9 ± 0.8	86.9 ± 0.7
5	−6.93	−8.5 ± 0.6	−8.8 ± 0.1	−8.8 ± 0.1	−8.8 ± 0.1	−8.8 ± 0.1
6	516.75	516.2 ± 9.9	515.2 ± 6.1	516.1 ± 3.8	516.8 ± 1.8	517.1 ± 0.9
7	354.60	351.1 ± 8.8	354.5 ± 2.8	354.88 ± 2	355.1 ± 1.4	355.2 ± 1.1
8	169.24	160.7 ± 12.2	165.8 ± 3.3	165.8 ± 2.1	165.7 ± 1.6	165.7 ± 1.3
9	88.90	85.5 ± 6.2	88.1 ± 1.7	88.1 ± 1.1	88.1 ± 0.8	88.1 ± 0.7
10	11.63	12.2 ± 0.8	12.5 ± 0.2	12.5 ± 0.1	12.5 ± 0.1	12.5 ± 0.1

FIGURE 13 Root mean square error (RMSE) as a function of the number of sensors in the input sensor network; (a) RMSE of the strains in [$\mu\varepsilon$] and the loads in [N]; (b) RMSE of the Loads 1 and the 2 in [N]

5 | CONCLUSIONS

In this work, a calibration matrix-based load monitoring is presented and successfully applied to an UAV. A limited number of sensors is exploited to initially reconstruct an equivalent load set consisting of concentrated forces applied to discrete saddles on the wings and to then reconstruct the full strain field in the UAV resulting from unknown flight maneuvers without requiring any training data set, thereby reducing the required effort for the real-life implementation of the method.

A least-squares minimization of an error functional defined as a comparison between discrete input strain measures, intrinsically function of the unknown load boundary condition, and a numerical formulation of the same, is used to reconstruct an equivalent load set. In particular, by exploiting the linearity, the functional minimization can be performed analytically, leading to a computationally very efficient procedure that can be operated online, since the calibration matrix inversion is done only once offline.

The numerical results prove the calibration matrix-based load monitoring algorithm can efficiently reconstruct the full-strain field in an aeronautical structure subjected to unknown flight maneuvers, without requiring any training data set. In particular, a proper strain field reconstruction is obtained exploiting discrete unidirectional input strain measures in the presence of complex unknown load boundary conditions despite a rather simple definition of the equivalent load set. Furthermore, the experimental results allow verifying the method's ability to cope with uncertainties, due to both noisy measurements and model simplification compared to the real platform. Thus, the results suggest the potential exploitation of the method for a realistic representation of complex aerodynamic fields by simplified lumped loads applicable in the laboratory.

Further testing will be devoted to verifying the method in the presence of dynamic disturbances, for example, engine vibrations. However, the physical pertinence of the reconstructed equivalent load set with reality is expected to decrease if very high-frequency disturbances produce a non-negligible effect on the input strain measurements, even though they do not interfere with the strain extrapolation by the algorithm. Furthermore, the exploitation of more complex equivalent load sets to better identify complex loading conditions in the view of the full strain and displacement fields reconstruction, and the validation of the method with real flight tests is a future research topic.

ORCID
Luca Colombo https://orcid.org/0000-0001-9355-099X

REFERENCES

1. Terroba F, Frövel M, Atienza R. Structural health and usage monitoring of an unmanned turbojet target drone. *Struct Heal Monit*. 2019; 18(2):635-650. https://doi.org/10.1177/1475921718764082

2. Ren L, Jiang T, Li D, Zhang P, Li H, Song G. A method of pipeline corrosion detection based on hoop-strain monitoring technology. *Struct Control Health Monit*. 2017;24(6):e1931. https://doi.org/10.1002/stc.1931

3. Jiang T, Ren L, Jia Z, Li D, Li H. Pipeline internal corrosion monitoring based on distributed strain measurement technique. *Struct Control Health Monit*. 2017;24(11):e2016. https://doi.org/10.1002/stc.2016

4. Cristiani D, Colombo L, Zielinski W, et al. On the evaluation of a coupled sequential approach for rotorcraft landing simulation. *Sensors (Switzerland)*. 2020;20(9):2540. https://doi.org/10.3390/s20092540

5. Zhao L, Huang X, Zhang Y, Zhu Y, Jia J, Zhu C. Aeolian vibration-based structural health monitoring system for transmission line conductors. *Struct Control Health Monit*. 2020;27(6):e2538. https://doi.org/10.1002/stc.2538

6. Todd MD. Data interrogation approaches with strain and load gauge sensor arrays. In: *Encyclopedia of Structural Health Monitoring*. 250 Williams Street NW Atlanta, GA 30303: American Cancer Society; 2009. https://doi.org/10.1002/9780470061626.shm012

7. Zhang C, Alam Z, Sun L, Su Z, Samali B. Fibre Bragg grating sensor-based damage response monitoring of an asymmetric reinforced concrete shear wall structure subjected to progressive seismic loads. *Struct Control Health Monit*. 2019;26(3):e2307. https://doi.org/10.1002/stc.2307

8. Staszewski W, Tomlinson G, Boller C, Tomlinson G. *Health Monitoring of Aerospace Structures*. Hoboken, New Jersey: Wiley Online Library; 2004.

9. Hunt SR, Hebden IG. Validation of the Eurofighter typhoon structural health and usage monitoring system. *Smart Mater Struct*. 2001;10 (3):497.

10. Reed SC. Development of a parametric-based indirect aircraft structural usage monitoring system using artificial neural networks. *Aeronaut J*. 2007;111(1118):209-230.

11. Holmes G, Sartor P, Reed S, Southern P, Worden K, Cross E. Prediction of landing gear loads using machine learning techniques. *Struct Heal Monit*. 2016;15(5):568-582. https://doi.org/10.1177/1475921716651809

12. Candon M, Levinski O, Altaf A, Carrese R, Marzocca P. Aircraft transonic buffet load prediction using artificial neural networks. In: AIAA Scitech 2019 Forum; 2019. https://doi.org/10.2514/6.2019-0763

13. Wada D, Sugimoto Y, Murayama H, Igawa H, Nakamura T. Investigation of inverse analysis and neural network approaches for identifying distributed load using distributed strains. *Trans Jpn Soc Aeronaut Space Sci*. 2019;62(3):151-161. https://doi.org/10.2322/tjsass.62.151

14. Fuentes R, Cross E, Halfpenny A, Worden K, Barthorpe RJ. Aircraft parametric structural load monitoring using Gaussian process regression. In: 7th European Workshop on Structural Health Monitoring, EWSHM 2014-2nd European Conference of the Prognostics and Health Management (PHM) Society; 2014:1933-1940. https://www.scopus.com/inward/record.uri?eid=2-s2.0-84939438509%26partnerID=40%26md5=8609fbbf7c6af0e6ffd49784da56ac53

15. He J, Zhou Y, Guan X, Zhang W, Wang Y, Zhang W. An integrated health monitoring method for structural fatigue life evaluation using limited sensor data. *Materials (Basel)*. 2016;9(11):894. https://doi.org/10.3390/ma9110894

16. He J, Zhou Y, Guan X, Zhang W, Zhang W, Liu Y. Time domain strain/stress reconstruction based on empirical mode decomposition: numerical study and experimental validation. *Sensors (Switzerland)*. 2016;16(8):1290. https://doi.org/10.3390/s16081290

17. Zou D, Zhao H, Liu G, Ta N, Rao Z. Application of augmented Kalman filter to identify unbalance load of rotor-bearing system: theory and experiment. *J Sound Vib*. 2019;463:114972. https://doi.org/10.1016/j.jsv.2019.114972

18. Wu A-L, Loh C-H, Yang JN, Weng J-H, Chen C-H, Ueng T-S. Input force identification: application to soil-pile interaction. *Struct Control Health Monit*. 2009;16(2):223-240. https://doi.org/10.1002/stc.308

19. Cumbo R, Tamarozzi T, Janssens K, Desmet W. Kalman-based load identification and full-field estimation analysis on industrial test case. *Mech Syst Signal Process*. 2019;117:771-785. https://doi.org/10.1016/j.ymssp.2018.08.045

20. Tessler A, Spangler JL. A least-squares variational method for full-field reconstruction of elastic deformations in shear-deformable plates and shells. *Comput Methods Appl Mech Eng*. 2005;194(2–5):327-339.

21. Colombo L, Sbarufatti C, Giglio M. Definition of a load adaptive baseline by inverse finite element method for structural damage identification. *Mech Syst Signal Process*. 2019;120:584-607. https://doi.org/10.1016/j.ymssp.2018.10.041

22. Gherlone M, Cerracchio P, Mattone M, Di Sciuva M, Tessler A. An inverse finite element method for beam shape sensing: theoretical framework and experimental validation. *Smart Mater Struct*. 2014;23(4):45027.

23. Kefal A. *Ocean Eng*. 2019;188:106262. https://doi.org/10.1016/j.oceaneng.2019.106262

24. Colombo L, Oboe D, Sbarufatti C, Cadini F, Russo S, Giglio M. Shape sensing and damage identification with iFEM on a composite structure subjected to impact damage and non-trivial boundary conditions. *Mech Syst Signal Process*. 2021;148:107163. https://doi.org/10.1016/j.ymssp.2020.107163

25. Cazzulani G, Di Gialleonardo E, Bionda S, Bassetti M, Crosio P, Braghin F. A new approach for the evaluation and the improvement of the metrological characteristics of an instrumented wheelset for the measure of wheel–rail contact forces. *Proc Inst Mech Eng Part F J Rail Rapid Transit*. 2017;231(4):381-393.

26. Bionda S, Di Gialleonardo E, Cazzulani G, Braghin F. Development of a new algorithm for wheel-rail contact force estimation using reduced measurement sets. In: Proceedings of the Mini Conference on Vehicle System Dynamics, Identification and Anomalies. Vol 2014-Janua; 2014:111-122. https://www.scopus.com/inward/record.uri?eid=2-s2.0-84988009631%26partnerID=40%26md5=299a4fec3fad59cad6d0d4dbbdcbf8fa

27. Airoldi A, Marelli L, Bettini P, Sala G, Apicella A. Strain field reconstruction on composite spars based on the identification of equivalent load conditions. In: Proceedings of SPIE - The International Society for Optical Engineering. Vol 10168; 2017. https://doi.org/10.1117/12.2260161

28. Airoldi A, Sala G, Evenblij R, et al. Load monitoring by means of optical fibres and strain gages. In: Smart Intelligent Aircraft Structures (SARISTU). Springer; 2016:433-469.

29. Piccolo A, Lecieux Y, Delepine-Lesoille S, Leduc D. Non-invasive tunnel convergence measurement based on distributed optical fiber strain sensing. *Smart Mater Struct.* 2019;28(4):045008. https://doi.org/10.1088/1361-665X/ab04cc

30. Skopinski TH, Aiken Jr WS, Huston WB. Calibration of strain-gage installations in aircraft structures for the measurements of flight loads. 1953.

31. Jebáček I, Horak M. Possibilities and methods of in-flight loading measurement. *Aviation.* 2012;16(2):47-50. https://doi.org/10.3846/16487788.2012.701860

32. Kwon H, Park Y, Kim J-H, Kim C-G. Embedded fiber Bragg grating sensor–based wing load monitoring system for composite aircraft. *Struct Heal Monit.* 2019;18(4):1337-1351. https://doi.org/10.1177/1475921719843772

33. Abdel-Jaber H, Glisic B. Monitoring of prestressing forces in prestressed concrete structures—an overview. *Struct Control Health Monit.* 2019;26(8):e2374. https://doi.org/10.1002/stc.2374

34. Zhang Z-F, Li Q, Liu H-W, Ding R. Optimal placement of strain sensors for urban rail vehicles based on information entropy [基于信息熵的城轨车辆应变传感器优化布置]. *Dongbei Daxue Xuebao/Journal Northeast Univ.* 2020;41(3):367-373 and 412. https://doi.org/10.12068/j.issn.1005-3026.2020.03.012

35. Zhao Y, Du J, Bao H, Xu Q. Optimal sensor placement for inverse finite element reconstruction of three-dimensional frame deformation. *Int J Aerosp Eng.* 2018;2018. https://doi.org/10.1155/2018/6121293

36. Huang Y, Ludwig SA. Sensor optimization using an evolutionary strategy for structural health monitoring in high temperature environments. In: Proceedings of SPIE - The International Society for Optical Engineering. Vol 10598.; 2018. https://doi.org/10.1117/12.2296565

37. Kurnyta A, Zielinski W, Reymer P, Dziendzikowski M, Dragan K. UAV pre-flight structural strength verification during on-ground static load test. In: 2019 IEEE International Workshop on Metrology for AeroSpace, MetroAeroSpace 2019 - Proceedings.; 2019:272-277. https://doi.org/10.1109/MetroAeroSpace.2019.8869596

38. Kurnyta A, Zielinski W, Reymer P, Dragan K, Dziendzikowski M. Numerical and experimental UAV structure investigation by pre-flight load test. *Sensors (Switzerland).* 2020;20(11):3014. https://doi.org/10.3390/s20113014

39. PANUKL. https://www.meil.pw.edu.pl/add/ADD/Teaching/Software/PANUKL